Nanoscale

ROYAL SOCIETY OF CHEMISTRY

MINIREVIEW

View Article Online
View Journal | View Issue

Cite this: *Nanoscale*, 2023, **15**, 11457

Recent advances in metal–organic framework/carbon nanotube nanocomposites for developing analytical applications†

Shereen A. Majeed

Received 7th March 2023,
Accepted 2nd June 2023

DOI: 10.1039/d3nr01074k

rsc.li/nanoscale

Nanoscience shows promise for scientific advancement in many sectors, such as biology, energy, materials, environment, and manufacturing. Nanocomposites are mixtures of two or more materials, one of which is nanosized particles. The composites are expected to show combined features resulting in general enhancements in their physical and chemical properties. Metal–organic frameworks (MOFs) are coordination polymers that have attracted attention from researchers in recent years due to their porosity and controllable functionality. Another example of interesting nanomaterials is carbon nanotubes (CNTs) which are also known for their mechanical and thermal properties. Incorporation of both these materials into a nanocomposite has shown an enhancement in properties and conquered challenges in the defects of construction. This mini-review sheds light on the recent synthetic approaches and characterization of MOF–CNT nanocomposites in order to access porous selective nanocomposites that can improve analyte detection in environmental matrixes and biological systems. A summary of the chemical composition of nanocomposites, analytes in the target, and analytical techniques used is provided.

Introduction

Carbon nanotubes (CNTs) are cylindrical tubes with π systems discovered by Lijima in 1991.[1] They are classified into single-walled carbon nanotubes (SWCNTs) and multi-walled carbon nanotubes (MWCNTs) according to the number of layers within the side walls. CNTs have been known for their high surface area and strong mechanical properties, as well as their uses in supercapacitors[2] and industrial applications.[3,4] They have been widely utilized in analyte extraction and modified electrodes due to their good conductivity as they assist in electron transfer between analytes and electrode surfaces.[5] Moreover, the hydrophobic nature of carbon nanotubes improves their ability to extract non-polar or weakly polar analytes.[6]

Metal–organic frameworks (MOFs), comprising metal nods coordinated to organic linker ligands, have also attracted the attention of researchers due to their high surface area, open metal active sites, and tunable functionalization which made them good candidates to be applied in catalysis,[7,8] drug delivery,[46,9] gas sensing,[10] and energy storage.[11] Furthermore, MOFs have the ability to interact with analytes through π–π stacking, different functional groups, metal sites, and van der Waals interactions.[12] The porosity of MOFs can also affect the selectivity of the analytes according to their shape and size.[13]

Approaches for preparing MOF–CNT nanocomposites

Three different methods have been utilized for preparing MOF/CNT nanocomposites as displayed in Fig. 1.

(a) *In situ* method: this method involves the addition of the MOF precursors with functionalized CNTs after dispersing CNTs in suitable solvents where metals start to coordinate with polar groups on the surface of CNTs, followed by coordination with organic linkers and the MOF growth process.[12,14–17] The experimental process is generally the same as the preparation process of MOFs, except that CNTs are added to the mixed solution. Mixing a metal salt with the CNT suspension for some time before adding an organic ligand helps with the diffusion of the metal to the surface of the CNTs. Characterization of nanocomposites afforded by this method depends on the formation of new characteristic peaks corresponding to MOF formation in the hybrid spectra, as illustrated in the section below.

(b) Carbonization method: here, a solid MOF acts as a single precursor of carbon sources of CNTs. The selected MOF

National Unit for Environmental Research and Services (NUERS), Research Sector, Kuwait University, P.O. Box 5969, Safat, 13060, Kuwait.
E-mail: sh.sh.a.majeed@gmail.com, shereen.abdulmajeed@ku.edu.kw

†Dedicated to the loving memory of Prof. Yehia A. Ibrahim. Chemistry Department – Kuwait University.

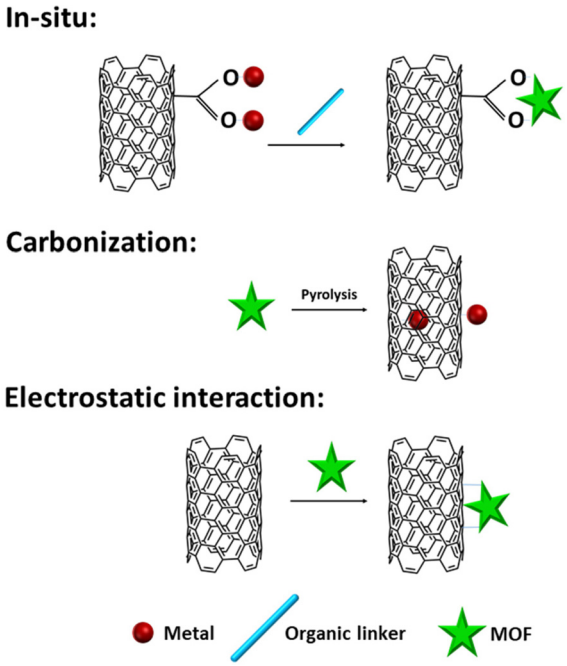

Fig. 1 General approaches for synthesizing MOF–CNT nanocomposites.

is typically pyrolyzed under an inert atmosphere at a high temperature of 300 °C for around 1 hour. The temperature is then gradually increased at a certain rate to 700–900 °C. In order to form CNTs doped with metallic atoms of the MOF precursor and nitrogen atoms, a nitrogen-containing organic linker, such as 2-methyl imidazole, was used.[6,18–20] The nanocomposite characterization confirms the carbonization with the appearance of new peaks, assigned to CNTs, in the nanocomposite spectra from different techniques, accompanied by the disappearance of peaks attributed to the MOF.

(c) Electrostatic interaction: it is a process by which the metal ions of an MOF are directly attached to functionalized CNT-COOH.[21–24] It is worth mentioning that the use of polyvinylpyrrolidone (PVP) as a capping agent for synthesizing ZIF-67 was found to contribute to successful electrostatic interactions between the MOF and CNTs.[22] The successful formation of nanocomposites is confirmed by analyzing the unaffected crystallinity of both the MOF and CNTs upon conjugation.

Characterization

Electron microscopy

Scanning electron microscopy (SEM), field emission scanning electron microscopy (FE-SEM), transmission electron microscopy (TEM), and high-resolution transmission electron microscopy (HR-TEM) are utilized for studying the morphology and specifying the shape, size, and structure of nanomaterials synthesized in the three different routes. The appearance of MOF crystals with CNTs in the *in situ* method confirms the success of the reaction of metal ions with organic linkers in the presence of CNTs, Fig. 2(A). Electron microscopy images show the cylindrical CNTs combined with the undistorted microstructure of MOFs in the case of electrostatic methodology, Fig. 2(B), while scans show the cylindrical shape of CNTs doped with heteroatoms when the nanocomposites are synthesized *via* MOF carbonization, Fig. 2(C). Additionally, the elemental analysis of nanohybrid surfaces can be performed using SEM which is surveyed by energy dispersive spectroscopy (EDS). Some examples are presented in Fig. 2.

X-Ray powder diffraction (XRD)

XRD is a powerful technique for characterizing the formation of crystalline nanocomposites. It is utilized for confirming the crystallinity of the synthesized hybrid and the stability of the chemical structure after analytical performance. New peaks corresponding to the MOF as well as the peaks corresponding to CNTs are expected to appear in XRD patterns to confirm the nanocomposite formation *via* the *in situ* method, Fig. 3(A). The electrostatic approach is confirmed by the appearance of unaffected peaks for both CNT and MOF upon conjugation, Fig. 3(B). Peaks corresponding to the MOF are expected to disappear, while new peaks corresponding to the CNT are expected to appear in the XRD pattern of nanocomposites synthesized *via* MOF pyrolysis as displayed in Fig. 3(C).

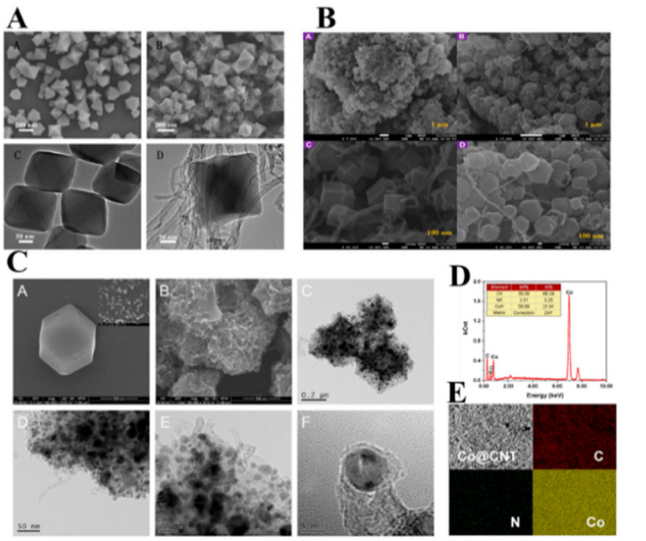

Fig. 2 (A) The morphology and structure of the MOF ((A) SEM and (C) TEM) and the nanohybrid synthesized *via* the *in situ* method ((B) SEM and (D) TEM). Reprinted with permission from ref. 5. Copyright 2021 Elsevier. (B) (A–D) FE-SEM images of MOF–MWCNTs prepared *via* the electrostatic approach. Reprinted with permission from ref. 22. Copyright 2021 Elsevier. (C) The SEM images of MOF ZIF-67 (A) and the nanohybrid Co@CNTs after MOF pyrolysis (B); the TEM images of Co@CNTs (C–E); the HRTEM images of Co@CNTs (F). (D) The EDS analysis of Co@CNTs. (E) The elemental mapping images of the C, N and Co elements of Co@CNTs. Reprinted with permission from ref. 18. Copyright 2020 Elsevier.

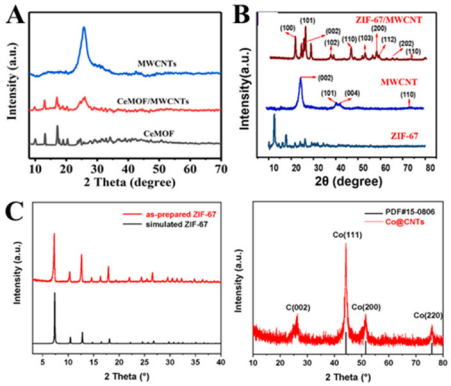

Fig. 3 (A) XRD patterns of MWCNTs, the MOF (CeMOF), and the nanocomposite (Co/NCNTs) synthesized *via* the *in situ* method, where new peaks corresponding to the MOF as well as the peaks corresponding to CNTs (2θ ∑26°) were reported. Reprinted with permission from ref. 26. Copyright 2022 Elsevier. (B) XRD patterns of the MOF (ZIF-67), MWCNTs, and the ZIF-67/MWCNT nanocomposite synthesized *via* the electrostatic method, where unaffected peaks for both the CNT and MOF upon conjugation were recorded. Reprinted with permission from ref. 22. Copyright 2021 Elsevier. (C) XRD patterns of (left) the MOF (ZIF-67) and (right) the corresponding nanocomposite after MOF pyrolysis (Co@CNTs), where peaks corresponding to the MOF disappear and new peaks corresponding to the CNT appear. Reprinted with permission from ref. 18. Copyright 2020 Elsevier.

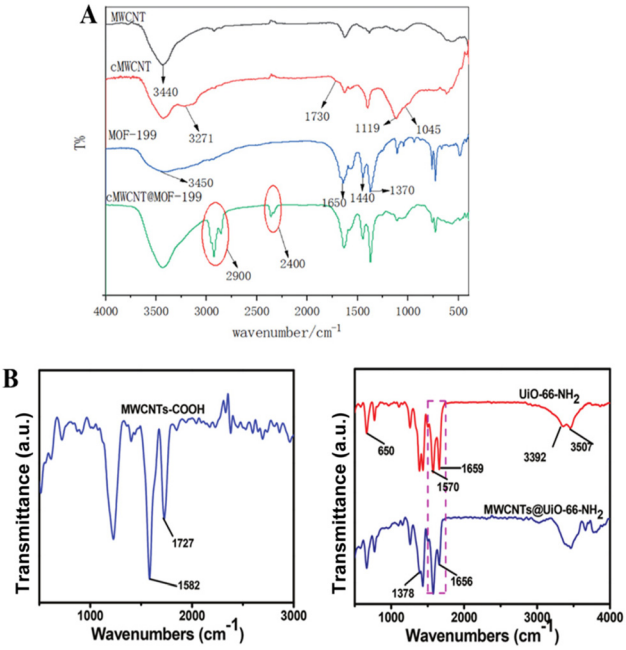

Fig. 4 FT-IR spectra of (A) MWCNTs, cMWCNTs, the MOF (MOF-199), and the nanohybrid cMWCNT/MOF-199. Reprinted with permission from ref. 25. Copyright 2021 the Royal Society of Chemistry. (B) FT-IR spectra of (lef): MWCNT-COOH, (right) MOF (UiO-66-NH_2) and the corresponding composite (MWCNT@UiO-66-NH_2). Reprinted with permission from ref. 16. Copyright 2021 the Royal Society of Chemistry 2020.

Fourier transform infrared (FT-IR) spectroscopy

FT-IR is utilized for confirming the presence of the functional groups in the nanohybrid and their interaction with the surroundings. Han *et al.* prepared carboxylated multi-walled carbon nanotubes (cMWCNTs) by functionalizing MWCNTs with the carboxyl group (–COOH). This was proved in the spectrum of cMWCNTs, which indicated the stretching vibration of –OH at 3271 cm^{-1}, stretching vibration of C═O at 1730 cm^{-1}, and a deformation vibration band of –OH at 1045 cm^{-1}, as demonstrated in Fig. 4(A). In the nanohybrid spectrum, an absorption frequency of –OH groups at a lower wave number (2400 cm^{-1}) was recorded and ascribed to the reduction of the bond force due to the coordination between the metal ions of the MOF and carboxylic groups on cMWCNTs. The absorption peak at 2900 cm^{-1} was attributed to the stretching vibration band from the strongly H-bonded COOH of cMWCNTs and the carboxylic group of 1,3,5-benzoic acid, the organic linker of the synthesized MOF.[25]

Han and co-workers reported a similar FT-IR spectrum of the nanohybrid synthesized *via* the *in situ* methodology to those of the corresponding MOF and CNTs. They ascribed the relative reduction in the NH_2 group band at 1656 cm^{-1} in the nanohybrid spectrum to the interaction of some free amino groups of the linker in the MOF framework with the carboxylic groups in MWCNT-COOH, as illustrated in Fig. 4(B).[16]

X-Ray photoelectron spectroscopy (XPS)

XPS is utilized for determining the elemental composition and chemical states of the nanohybrid to be compared with its precursors. For instance, Liu and co-workers prepared ZIF-67 by the coordination of 2-methylimidazole with Co(II) in the presence of CNTs. XPS patterns exhibited three peaks corresponding to C═O, C–O, and O–C═O bonds at 531.6, 532.1, and 533.3 eV, respectively, confirming the electrostatic attraction between the MOF and the CNT during the growth of MOF crystals, as presented in Fig. 5(A).[27] Meanwhile, in the electrostatic approach, no new characteristic peak was recorded upon conjugation. However, the peak intensity of C 1s was expected to significantly enhance, as displayed in Fig. 5(B).[5]

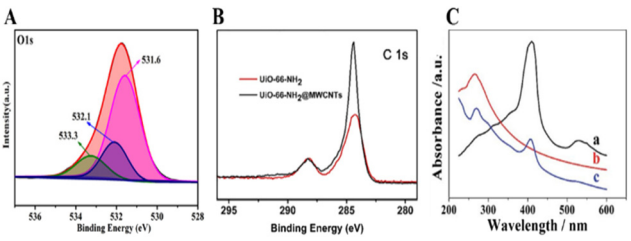

Fig. 5 XPS spectra of (A) O 1s for the nanohybrid ZIF-67-w-CNTs. Reprinted with permission from ref. 27. Copyright 2022 Elsevier. (B) XPS spectra of C 1s for the MOF (UiO-66-NH_2) and UiO-66-NH_2@MWCNTs. Reprinted with permission from ref. 5. Copyright 2021 Elsevier. (C) UV-Vis diagrams of (a) Cyt c, (b) MWCNTs, and (c) Cyt c-MWCNTs. Reprinted with permission from ref. 21. Copyright 2021 the Royal Society of Chemistry.

UV-Vis spectroscopy

Although UV-Vis was not widely utilized for characterizing the MOF–CNT nanohybrids, it was utilized for confirming the bonding of other materials to CNTs including cytochrome c (Cyt c). As displayed in the Cyt c spectrum, the Q and B bands of porphyrin, a component of Cyt c, at 530 and 410 nm disappeared and slightly blue-shifted in the Cyt c-MWCNT spectrum, respectively, in addition to the absorption at 265 nm considered as a characteristic band for the CNT (Fig. 5(C)).[21]

MOF–CNT analytical performance

The stability of MOF structures is related to their ability to maintain their long-range ordered structures in a certain chemical environment. Three main categories of stabilities, namely chemical, thermal, and mechanical stabilities, are ascribed to MOFs in different applications. Analytical applications are performed in acidic and/or basic aqueous media, and the structure of MOFs could be altered, which makes evaluating MOF stability of great importance. The effects of bases, acids, and buffers on MOF stability are explained elsewhere.[28–30] Water is the most common matrix in aqueous samples. Water molecules can coordinate with metal sites in MOFs, which might result in the formation of protonated organic linkers and metal hydroxides depending on the coordination bond strength between organic linkers and metal ions. This undesirable water–MOF coordination might increase in acidic and basic solutions. The presence of protons or hydroxide ions in the distorted structures of MOFs can promote the electrophilic or nucleophilic attack of the metal centers on the coordination bonds with different reagents other than water that include the -OH group and thus lead to the degradation of MOFs.[31–33] The stability of MOFs in water has attracted enormous attention and been reported in comprehensive reviews.[30,34,35]

Li *et al.* investigated the analytical performance of ascorbic acid by a nanohybrid. In spite of the fact that the authors reported the stability of the crystal structure during sensing through similar XRD patterns of the composite before and after sensing, a slight broadening with a small shift to a lower angle was observed, as illustrated in Fig. 6(A).[12] This could be

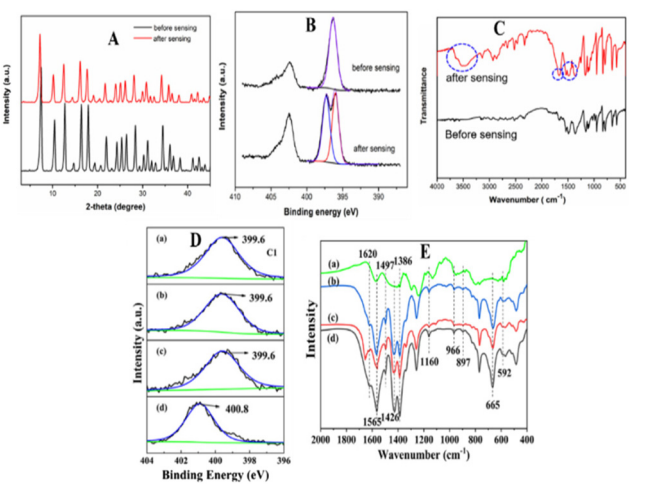

Fig. 6 (A) XRD of the nanocomposite (ZIF-65@CNTs) before and after AA sensing. (B) XPS spectra of N 1s of the nanocomposite (ZIF-65@CNT) before and after electrochemical sensing of ascorbic acid. (C) FT-IR spectra of the nanocomposite (ZIF-65@CNT) before and after the electrochemical sensing of ascorbic acid. Reprinted with permission from ref. 12. Copyright 2020 Elsevier. (D) N 1s pattern (d) before and after (a) PAH extraction of pyrene, (b) fluoranthene, and (c) phenanthrene. (E) FT-IR spectra of (a) UiO-66-NH_2, (b) MWCNT/UiO-66-NH_2, (c) etched MWCNT/UiO-66-NH_2, and (d) simulated UiO-66-NH_2. Reprinted with permission from ref. 36. Copyright 2020 Springer.

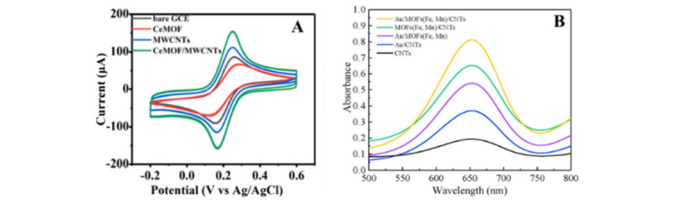

Fig. 7 (A) Cyclic voltammetry (CV) curves of bare glassy carbon electrode (GCE) and GCE modified by the synthesized MOF (CeMOF), MWCNTs, and nanohybrid CeMOF/MWCNTs. The best current response was noticed when the electrode is modified with the nanohybrid. Reprinted with permission from ref. 26. Copyright 2022 Elsevier. (B) The UV-Vis spectra of the catalytic activity of CNTs, gold nanoparticles (Au NPs), MOFs (Fe, Mn)/CNTs, Au/MOFs (Fe, Mn), Au/CNTs, and Au/MOFs (Fe, Mn)/CNTs towards peroxidase-like detection. Reprinted with permission from ref. 14. Copyright 2020 Elsevier.

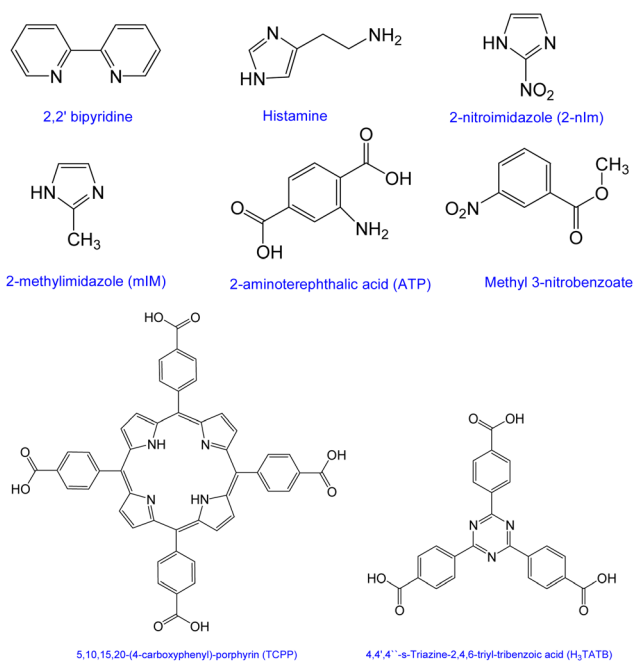

Fig. 8 Chemical structures of the organic linkers of MOF precursors in recently reported MOF–CNT hybrids.

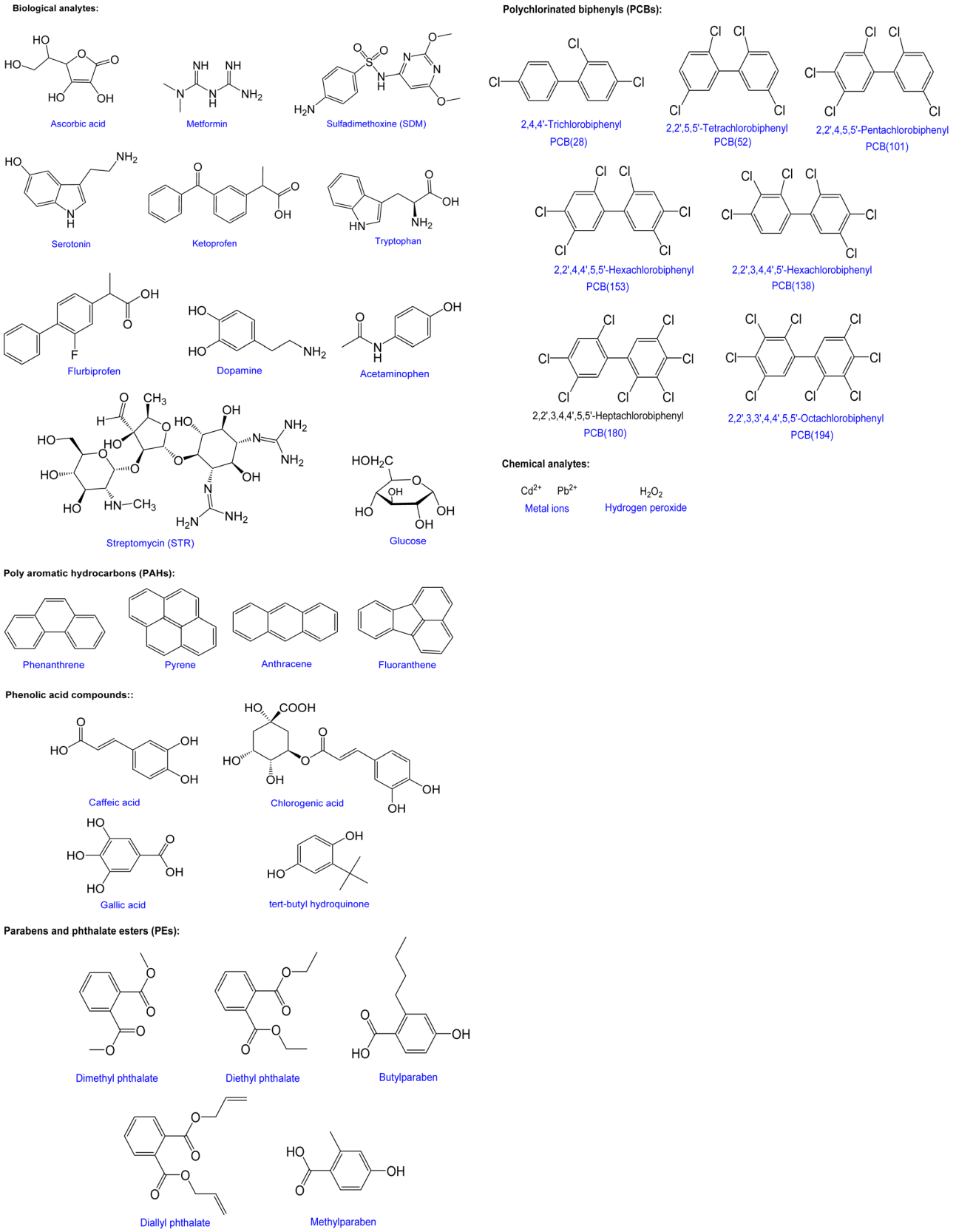

Fig. 9 The general chemical structures of analytes detected recently using MOF–CNT nanocomposites.

Table 1 Overview of the recent CNT based metal–organic frameworks in analyte detection

Nanocomposite system	MOF precursors	Analytical technique	Analytes	Linear range	Detection limit	Sample	Ref.
ZIF-67N-doped CNT	$Co(NO_3)_2{\cdot}6H_2O$ 2-Methylimidazole (mIM)	SPME-fiber GC-MS	PCB(28) PCB(52) PCB(101) PCB(153) PCB(138) PCB(180) PCB(194)	0.5–1000.0 ng L^{-}· 0.3–1000.0 ng L^{-1} 0.3–1000.0 ng L^{-1} 0.3–1000.0 ng L^{-1} 0.5–1000.0 ng L^{-1} 0.3–1000.0 ng L^{-1} 0.5–1000.0 ng L^{-1}	0.57 ng L^{-}· 0.42 ng L^{-1} 0.47 ng L^{-1} 0.33 ng L^{-1} 0.54 ng L^{-1} 0.45 ng L^{-1} 0.72 ng L^{-1}	River water	6
MMWCNTs@MIL-101(Cr) (Fe_3O_4)	$(Cr(NO_3)_3$-$9H_2O$ $FeCl_3$ ($(NH_4)_2Fe(SO_4)_2{\cdot}6H_2O$ terephthalic acid (H_2BDC) = 1,4-benzene dicarboxylic acid	Dispersive magnetic micro solid-phase extraction (D_SPE-HPLC-DAD)	-Dimethyl phthalate -Diethyl phthalate -Diallyl phthalate -Methylparaben -Butylparaben	0.1–1500 μg L^{-1} 0.5–1500 μg L^{-1} 0.2–1500 μg L^{-1} 0.5–1500 μg L^{-1} 0.3–1500 μg L^{-1}	0.03 μg L^{-1} 0.15 μg L^{-1} 0.06 μg L^{-1} 0.15 μg L^{-1} 0.09 μg L^{-1}	Water, cream	15
Copper porphyrin metal organic frameworks (Cu-MOFs) and Au@Ag core–shell nanoparticles decorated with MWCNTs	$Cu(NO_3)_2{\cdot}3{\cdot}H_2O$ TCPP = 5,10,15,20-(4-carboxyphenyl)-porphyrin (TCPP)	Electrochemistry	-Acetaminophen, -Dopamine	1–500 μM 0.6–300 μM	0.232 μM 0.082 μM	Human serum, urine	23
ZIF-65@CNT electrode ZIF-65	$Zn(CH_3COO)_2$, $2H_2O$ 2-nitroimidazole (2-nIm)	Electrochemistry	Ascorbic acid	200–2267 μM	1.03 μM	Phosphate buffer solution (PBS)	12
Au/MOFs(Fe, Mn)/CNTs	$FeCl_3{\cdot}6H_2O$ $MnCl_2$ 2-Aminoterephthalic acid (NH_2-BDC)	UV-Vis	-H_2O_2 -Glucose -Sulfadimethoxine (SDM)	0.34–53.05 nM 0.005–0.3 μM 0.54–41.58 μg L^{-1}	0.18 nM 0.002 μM 0.35 μg L^{-1}	Water, living organisms, blood, antibiotics	14
MWCNTs/PANI/ZIF-67	$Co(NO_3)_2{\cdot}6H_2O$ 2-Methylimidazole	SPME stainless steel wire/GC-FID	-Naphthalene -Fluorene -Phenanthrene -Anthracene	0.005–1000.0 μg L^{-1} 0.005–100.0 μg L^{-1} 0.005–500.0 μg L^{-1} 0.005–100.0 μg L^{-1}	0.3 μg L^{-1} 0.8 μg L^{-1} 0.5 μg L^{-1} 0.5 μg L^{-1}	Borage Chamomile Black tea Green tea Tab water Well water Sea water Aqueduct water	41
UiO-66-NH_2	$ZrCl_4$	Electrochemistry	Lead ions	0.001–0.8 μmol L^{-1}	0.5 nmol L^{-1}	Tap water, lake water	16
With COOH-CNTs (Co/NCNTs)	2-Aminoterephthalic acid $Co(NO_3)_2{\cdot}6H_2O$ 2-Methylimidazole	Electrochemistry	*tert*-Butyl hydroquinone	0.05–80.00 lmol L^{-1}	10 nmol L^{-1}	Soybean oil, sesame oil	20
PANI-etched MWCNT/UiO-66NH_2	$ZrCl_4$ Aminoterephthalic acid (ATP)	SPME fiber/HPLC-PAD	-Phenanthrene -Fluoranthene -Pyrene	0.05–20 ng mL^{-1}	10 pg mL^{-1}	Lake water	36
MOF-818@RGO/MWCNTs	$Cu(NO_3)_2{\cdot}3{\cdot}H_2O$ $ZrOCl_2{\cdot}8H_2O$ 1*H*-Pyrazole-4-carboxylic acid	Electrochemistry	-Caffeic acid -Chlorogenic acid -Gallic acid	0.2–7 μM 7–50 μM 0.1–3 μM	0.0052 μM 0.0057 μM 0.18 μM	Human serum, urine	24
Co@CNTs	$Co(NO_3)_2{\cdot}6H_2O$ 2-Methylimidazole	HPLC-UV	-Flurbiprofen -Ketoprofen	5.0–1000 ng L^{-1}	0.60 ng L^{-1} 0.70 ng L^{-1}	Human serum	18

Table 1 *(Contd.)*

Nanocomposite system	MOF precursors	Analytical technique	Analytes	Linear range	Detection limit	Sample	Ref.
CNT-Cu-MOF	$Cu(NO_3)_2{\cdot}3H_2O$ Methyl 3-nitrobenzoate	Electrochemistry	Cadmium ions	0.2–10 μM	0.275 nM	Tap water	17
Cyt c-MWCNTs and Co-MOFs/AuNPs	$Co(NO_3)_2{\cdot}6H_2O$ 2-Aminoterephthalic acid (NH_2-BDC)	Electrochemistry	Nitrite	0.005–1000 mmol L^{-1}	0.0044 mmol L^{-1}	Sausage, apple	21
cMWCNT/MOF-199	$Cu(NO_3)_2{\cdot}3H_2O$	Electrochemistry	3-Chloro-1,2-propanediol (3-MCPD)	1.0^{-9}–10^{-5} mol L^{-1}	4.3×10^{-10} mol L^{-1}	Soy sauce	25
Chiral metalorganic frameworks (CMOFs)/MWCNT	1,3,5-Benzoic acid $CuSO_4{\cdot}3H_2O$ 2-Thienyl-formaldehyde L-Phenylalanine	Electrochemistry	Tryptophan (TRP)	0.4 μM–19 μM	0.11 μM for L-Trp 0.16 μM for D-Trp	N/A	42
NCNT-MOF CoCu	$CuNO_3{\cdot}3H_2O$ $Co(NO_3)_2{\cdot}6H_2O$ 2-Methylimidazole	Electrochemistry	-Glucose -Hydrogen peroxide	0.05–2.5 mM 0.05–3.5 mM	0.15 μM 0.206 μM	Blood serum	19
ZIF-67/MWCNTs	$Co(NO_3)_2{\cdot}6H_2O$ Methyl imidazole	Electrochemistry	Serotonin	0.049 μM–800 μM	7 nM	Human urine, blood serum	22
UiO-66-NH2@MWCNTs	$ZrCl_4$ 2-Aminoterephthalic acid	ICP-MS	Cd^{2+}	0.5–170 μg L^{-1}	0.2 μg L^{-1}	Meat	5
CeMOF/MWCNTs	$Ce(NO_3)_3{\cdot}6H_2O$ Sulfanilic acid	Electrochemistry	Gallic acid	1.5 μM–200 μM	0.14 μM	Green tea	26
Au@poly(diallyldimethylammonium chloride)NCNT/polyethyleneimine-functionalized with MIL-101(Cr)	$Cr(NO_3)_3{\cdot}9H_2O$ Terephthalic acid (TPA)	Electrochemistry	Streptomycin (STR)	0.01–250 nM	2.31 nM	Milk	43

attributed to the slight distortion of the diffraction planes of nanocomposite crystals upon ascorbic acid extraction.

It was demonstrated that when utilizing nitro groups in the organic linker for synthesizing an MOF, these groups can interact with analytes as shown in the XPS pattern of N 1s of the nanocomposite after analyte detection, where the peak shifted from 395.93 eV before sensing to 397.41 eV after sensing, accompanied by a partial splitting into another peak (Fig. 6(B)).[12] Furthermore, two new bands at 3487 and 1662 cm^{-1} were exhibited in the FT-IR spectrum of the nanocomposite, ascribed to the stretching and vibrations of N–H bonding, respectively, giving evidence of hydrogen bond formation between the nitro groups of the MOF and the hydrogen atoms of the analyte (ascorbic acid) (Fig. 6(C)).[12]

Chen *et al.* reported π–π interaction between a composite and polyaromatic hydrocarbon (PAH) *via* the nitro group of linkers in UiO-66-NH_2. The XPS pattern of the nanocomposite exhibited a shift in the N 1s peak from 400.8 eV before detection to 399 eV after detection, as displayed in Fig. 6(D). This reduction in the electron binding energy of the inner layer indicated that the outer electron density of N was increased due to PAH absorption and confirmed the anion–π interaction between the negatively charged amino group on the composite and PAHs. In addition, the absorption of (Ar–N) in the FT-IR spectrum of the hybrid increased after PAH extraction. Moreover, the absorption peak corresponding to C=C in the nanocomposite spectrum was also noticed to increase after extraction confirming the π–π interaction between the composite and PAH, as presented in Fig. 6(E).[36]

Further modification to enhance the analytical performance

Promising features of MOFs and CNTs together were found to enhance the sensitivity of analyte detection in comparison with the use of MOFs and CNTs alone (Fig. 7(A)).[26] Although different organic linkers have been utilized for synthesizing MOFs (Fig. 8), more enhancement could still be recorded when the nanohybrid is fabricated with other nanomaterials and/or different structures of functional groups (Fig. 7(B)).[14]

For instance, Yan *et al.* applied reduced graphene oxide (RGO) to MOF–CNT nanocomposites to improve the electrochemical sensing performance, where GO could facilitate electron transfer and prevent MOF accumulation.[24] An electrochemical biosensor of nitrite was improved by involving the cytochrome c enzyme due to its role in electron transfer in oxidoreductase enzymes in organisms.[21] Other approaches for MOF–CNT nanocomposite fabrication were utilized for enhancing the conductivity of electrosensors such as using iron oxide (Fe_3O_4) nanoparticles that can facilitate electron transfer due to their inverse spinel structure,[37] in addition to immobilizing gold–silver core shell nanoparticles in which their plasmonic properties contribute to interaction with a wide range of analytes.[23,38,39]

Nitrogen-doped carbon nanotubes (NCNTs) have also been reported to promote the electron transport properties for the electrochemical sensitive detection of phenolic acids.[20] Moreover, NCNTs showed an increase in the porosity and active sites of the sorbent to enhance the extraction. Guo *et al.* utilized the gluing method to coat a stainless steel wire with zeolitic imidazole framework-67 (ZIF-67) derived NCNTCs used in solid phase microextraction (SPME) for seven polychlorinated biphenyls (PCBs) through the use of gas chromatography-mass spectrometry (GC-MS), as shown in Fig. 9.[6] ZIF-67 was found to be poorly immobilized on the steel wire to be used as a sorbent for SPME. In order to overcome this problem, Hajializadeh *et al.* prepared an SPME stainless steel wire *via* layer-by-layer electrodeposition and incorporated the conductive polymer polyaniline (PANI). This polymer is utilized in anticorrosive coating on various metals due to the inter-chain hydrogen bonding which makes it difficult for a solvent to pass through the chains and, hence, stabilizes the fiber coating.[40] The fabricated stainless steel wire was then tested to extract PAH in aqueous samples and subjected to gas chromatography-flame ionization detection (GC-FID). Chen *et al.* utilized a similar strategy for enhancing the extraction efficiency of UiO-66-CNT towards PAH in water, which was detected by high-performance liquid chromatography (HPLC).[36] A summary of the current studies is outlined in Table 1. The general chemical structures of analytes detected recently with MOF–CNT nanocomposites are presented in Fig. 9.

Concluding remarks

MOF–CNT nanocomposites have attracted the attention of researchers for analytical applications due to their multi-reactive sites toward the analytes. MOFs can interact with the analytes through the metal sites and/or the functional groups of the organic linkers, whereas CNTs interact with the analytes *via* π–π interactions and van der Waals forces. In the current mini-review, we highlighted the recent approaches to produce MOF–CNT nanocomposites. Characterization by various techniques was also demonstrated to confirm the different strategies of nanocomposite synthesis. A summary of different recent fabrications for the nanocomposites and their analytical application *versus* different analytes was presented.

From a near-future perspective, further studies are still needed to investigate other factors that influence the sorbent/sensor interaction with analytes such as pore volume and pore size. For example, ZIF-67 has been widely used in MOF–CNT nanocomposites; in spite of that, neither the effect of polymorphism nor the microstructures of other zeolitic imidazolate frameworks, ZIFs, have yet been studied in analytical chemistry.

Additionally, a further nanohybrid modification can be applied to increase the porosity, such as immobilizing by the sol–gel technology.

Particular attention has been paid to the stability of the MOF–CNT nanocomposites. Although some examples under harsh chemical conditions (acidic or alkaline media) are reported, such as AlTCS-1, which showed strong chemical resistance in aqua regia solution over 24 h,[44] and PCN-601, whose structure was not distorted upon alkaline treatment in a saturated NaOH solution at 100 °C,[45] more studies are still needed to intensively examine the stability of MOF–CNT nanocomposites to optimize the best analyte extraction and detection and hence avoid the difficulties in nanocomposite recycling/regeneration.

More developments are needed to functionalize CNTs with polar groups in order to enhance their dispersion in organic solvents and water samples. More efforts are still required to approach green chemistry in MOF–CNT synthesis.

Conflicts of interest

There are no conflicts of interest to declare.

Acknowledgements

The current study received no financial support.

References

1 S. Iijima, *Nature*, 1991, **354**, 56–58.
2 S. H. Aboutalebi, A. T. Chidembo, M. Salari, K. Konstantinov, D. Wexler, H. K. Liu and S. X. Dou, *Energy Environ. Sci.*, 2011, **4**, 1855–1865.
3 M. Morsy, A. I. Abdel-Salam, D. A. Rayan, I. Gomaa and A. Elzwawy, *J. Nanopart. Res.*, 2022, **24**, 226.
4 Q. H. Nguyen, V. T. Luu, S. N. Lim, Y.-W. Lee, Y. Cho, Y.-S. Jun, M. H. Seo and W. Ahn, *ACS Appl. Mater. Interfaces*, 2021, **13**, 28036–28048.
5 X. Wang, Y. Xu, Y. Li, Y. Li, Z. Li, W. Zhang, X. Zou, J. Shi, X. Huang and C. Liu, *Food Chem.*, 2021, **357**, 129762.
6 Y. Guo, X. He, C. Huang, H. Chen, Q. Lu and L. Zhang, *Anal. Chim. Acta*, 2020, **1095**, 99–108.
7 H. Konnerth, B. M. Matsagar, S. S. Chen, M. H. Prechtl, F.-K. Shieh and K. C.-W. Wu, *Coord. Chem. Rev.*, 2020, **416**, 213319.
8 U. Khan, A. Nairan, J. Gao and Q. Zhang, *Small Struct.*, 2023, **4**, 2200109.
9 J. Cao, X. Li and H. Tian, *Curr. Med. Chem.*, 2020, **27**, 5949–5969.
10 Y. M. Jo, Y. K. Jo, J. H. Lee, H. W. Jang, I. S. Hwang and D. J. Yoo, *Adv. Mater.*, 2022, 2206842.
11 J. Ren, Y. Huang, H. Zhu, B. Zhang, H. Zhu, S. Shen, G. Tan, F. Wu, H. He and S. Lan, *Carbon Energy*, 2020, **2**, 176–202.
12 Y. Li, W. Ye, Y. Cui, B. Li, Y. Yang and G. Qian, *J. Mol. Struct.*, 2020, **1209**, 127986.
13 L. Xiao, R. Xu, Q. Yuan and F. Wang, *Talanta*, 2017, **167**, 39–43.
14 X. Dang and H. Zhao, *Talanta*, 2020, **210**, 120678.

15 N. Jalilian, H. Ebrahimzadeh and A. A. Asgharinezhad, *J. Chromatogr., A*, 2019, **1608**, 460426.
16 X. Sun, Y. Chen, Y. Xie, L. Wang, Y. Wang and X. Hu, *Analyst*, 2020, **145**, 1833–1840.
17 S. Singh, A. Numan, H. Somaily, M. M. Dawsari, M. H. S. Alqarni, A. Alam and P. Kumar, *J. Environ. Chem. Eng.*, 2021, **9**, 106534.
18 W. Wu, F. Lin, X. Yang, B. Wang, X. Lu, Q. Chen, F. Ye and S. Zhao, *Talanta*, 2020, **207**, 120284.
19 S. E. Kim and A. Muthurasu, *Electroanalysis*, 2021, **33**, 1333–1345.
20 J. Tang, S.-B. Zheng, S.-X. Jiang, J. Li, T. Guo and J.-H. Guo, *Rare Met.*, 2021, **40**, 478–488.
21 S. Huang, M. Lu and L. Wang, *RSC Adv.*, 2021, **11**, 501–509.
22 N. Nataraj, T.-W. Chen, S. M. Chen, T.-W. Tseng, Y. Bian, T.-T. Sun and J. Jiang, *J. Taiwan Inst. Chem. Eng.*, 2021, **129**, 299–310.
23 W. Yao, H. Guo, H. Liu, Q. Li, R. Xue, N. Wu, L. Li, M. Wang and W. Yang, *J. Electrochem. Soc.*, 2019, **166**, B1258.
24 Y. Yan, X. Bo and L. Guo, *Talanta*, 2020, **218**, 121123.
25 S. Han, Y. Ding, F. Teng, A. Yao and Q. Leng, *RSC Adv.*, 2021, **11**, 18468–18475.
26 J. Chen, Y. Chen, S. Li, J. Yang and J. Dong, *Colloids Surf., A*, 2022, **650**, 129318.
27 L. Liu, Y. Gao, Y. Liu, M. Xu, S. Yang, K. Li, S. Zhao, D. Cao and J.-H. Ahn, *Appl. Surf. Sci.*, 2022, **593**, 153417.
28 F. Luo, *J. Phys.: Conf. Ser.*, 2021, **1939**, 012051.
29 H. Bunzen, *ChemNanoMat*, 2021, **7**, 998–1007.
30 M. Ding, X. Cai and H.-L. Jiang, *Chem. Sci.*, 2019, **10**, 10209–10230.
31 E. Moumen, A. H. Assen, K. Adil and Y. Belmabkhout, *Coord. Chem. Rev.*, 2021, **443**, 214020.
32 N. u. Qadir, S. A. M. Said and H. M. Bahaidarah, *Microporous Mesoporous Mater.*, 2015, **201**, 61–90.
33 K. Leus, T. Bogaerts, J. De Decker, H. Depauw, K. Hendrickx, H. Vrielinck, V. Van Speybroeck and P. Van Der Voort, *Microporous Mesoporous Mater.*, 2016, **226**, 110–116.
34 B. Liu, K. Vikrant, K.-H. Kim, V. Kumar and S. K. Kailasa, *Environ. Sci.: Nano*, 2020, **7**, 1319–1347.
35 X. Liu, X. Wang and F. Kapteijn, *Chem. Rev.*, 2020, **120**, 8303–8377.
36 J. Chen, B. Zhang, X. Dang, D. Zheng, Y. Ai and H. Chen, *Microchim. Acta*, 2020, **187**, 1–9.
37 S. Yuan, X. Bo and L. Guo, *Talanta*, 2019, **193**, 100–109.
38 S. A. Majeed, *Analyst*, 2020, **145**, 6744–6752.
39 S. A. Majeed, K. E. Sekhosana and A. Tuhl, *Arabian J. Chem.*, 2020, **13**, 8848–8887.
40 A. Abdelraheem, A. H. El-Shazly and M. F. Elkady, *Alexandria Eng. J.*, 2018, **57**, 3291–3297.
41 A. Hajializadeh, M. Ansari, M. M. Foroughi and M. Kazemipour, *Microchem. J.*, 2020, **157**, 105008.
42 X. Wei, L. Li, H. Lian, X. Cao and B. Liu, *J. Electroanal. Chem.*, 2021, **886**, 115108.
43 Y. Hui, D. Yang, W. Wang, Y. Liu, C. He and B. Wang, *Food Chem.*, 2023, **402**, 134150.
44 Y. Guo, J. Zhang, L.-Z. Dong, Y. Xu, W. Han, M. Fang, H.-K. Liu, Y. Wu and Y.-Q. Lan, *Chem. – Eur. J.*, 2017, **23**, 15518–15528.
45 K. Wang, X.-L. Lv, D. Feng, J. Li, S. Chen, J. Sun, L. Song, Y. Xie, J.-R. Li and H.-C. Zhou, *J. Am. Chem. Soc.*, 2016, **138**, 914–919.
46 Edward Sekhosana, Kutloano, *Coordination Chemistry Reviews*, 2023, **491**, 215232, DOI: **https://doi.org/10.1016/j.ccr.2023.215232**.